Inorganic Chemistry

Article

pubs.acs.org/IC

A Crystal Structure Analysis and Magnetic Investigation on Highly Ordered Mesoporous Cr_2O_3

Harun Tüysüz, Claudia Weidenthaler, Tobias Grewe, Elena Lorena Salabaş,[†] Maria. J. Benitez Romero, and Ferdi Schüth*

Max-Planck-Institut für Kohlenforschung, Kaiser-Wilhelm-Platz 1, D-45470 Mülheim an der Ruhr, Germany

ABSTRACT: A series of highly ordered mesoporous Cr_2O_3 were prepared through the nanocasting pathway from decomposition of chromium(VI) oxide using KIT-6 as a hard template. The effects of the calcination temperature on the crystal structure, textural parameters and magnetic properties of the material were investigated. It was found that with increasing calcination temperature, surface area and pore volume of the mesoporous Cr_2O_3 decreased slightly. Unpredictably, increasing calcination temperature also influences the lattice parameters of the Cr_2O_3 crystal, and this rearrangement in the lattice parameter leads to changes in the value of the Néel temperature. A spin-flop transition has been observed at a magnetic field smaller than that of bulk material.

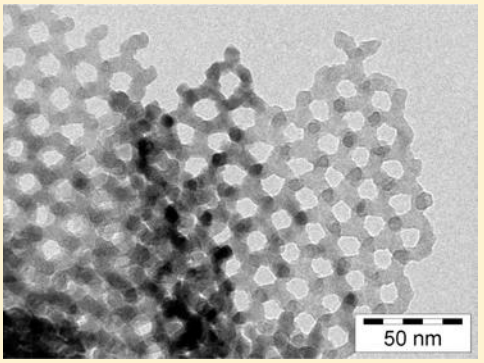

1. INTRODUCTION

Ordered mesoporous materials have been comprehensively investigated in the past two decades due to their unique properties such as high surface areas, uniform pore sizes, tunable pore structures, geometries and compositions. Nanocasting (hard templating) is a very effective method to prepare ordered mesoporous materials that are usually difficult to synthesize by conventional pathways (soft templating).[1] Ordered nanostructured metal oxides can be obtained in a three-step procedure from silica template via the nanocasting pathway. After synthesis of the template, the template itself can be impregnated with an appropriate metal precursor, followed by calcination. Finally, the mesoporous metal oxide product can be obtained after removal of silica with diluted HF or NaOH. The preparation and application of these materials are covered in several recent reviews.[2−6] The mesoporous metal oxides synthesized by this method are highly crystalline, have high surface areas and can possess interesting magnetic properties. Following this method, several non-silica based oxides like Co_3O_4,[7,8] Fe_3O_4,[9] 2-line ferrihydrite,[10] NiO,[11,12] In_2O_3,[12] Mn_2O_3,[12,13] Mn_3O_4,[13] MnO_2,[14] CeO_2,[15] MgO,[16] CuO[17] and CoO[18,19] have successfully been synthesized. The particle size, surface area, morphology and geometry of the replica can be tuned to a certain extent by varying the textural parameters of the parent silica and the synthetic parameters such as type of precursor, impregnation method, loading times and amount, type of the container, drying method and calcination method.[20,21]

Chromium forms several oxides; the best known ones are chromium(VI) oxide, CrO_3, and chromium(III) oxide, Cr_2O_3. In nature, Cr_2O_3 occurs as the rare mineral eskolaite that is found in chromium-rich tremolite skarns, metaquartzites and chlorite veins. It has a corundum crystal structure consisting of a hexagonal close packed array of oxide anions with 2/3 of the octahedral holes occupied by chromium. Cr_2O_3 powders have a range of applications especially as a green pigment in industry and as an important catalyst in dehydrogenation[22] and chlorine/fluorine (Cl/F) exchange reactions for the production of chlorofluorocarbon alternatives.[23] Mesoporous Cr_2O_3 has been prepared from different templates and precursors via nanocasting. Zhu et al. reported the synthesis of Cr_2O_3 using modified SBA-15 as the hard template and $H_2Cr_2O_7$ as the chromium precursor.[24] The preparation of Cr_2O_3 single crystals from KIT-6 and $Cr(NO_3)_3{\cdot}9H_2O$ was reported by the same group.[25] Recently, the Cr_2O_3 replicas from the 2D hexagonal SBA-15 and 3D cubic KIT-6 were also obtained from a vacuum assisted solvent evaporation method by using $Cr(NO_3)_3{\cdot}9H_2O$.[26] Zhao et al. demonstrated an ammonia nitridation approach to synthesize ordered mesoporous CrN from mesostructured Cr_2O_3 that was prepared via a nanocasting route by using mesoporous silica SBA-15 as the hard template.[27] Fabrication of cubic ordered Cr_2O_3 was also accomplished by Sinha et al. through a soft templating route using triblock copolymer F-127 as template and chromium nitrate as precursor.[28] Recently Hill et al. reported on crystallographic and magnetic studies of mesoporous Cr_2O_3. Their neutron diffraction analysis indicated that the magnetic and crystallographic properties of nanocast Cr_2O_3 are identical to bulk Cr_2O_3.[29]

Cr_2O_3 is a low-anisotropy easy-axis antiferromagnet (AF) with a Néel temperature of 307 K. Below the Néel transition temperature in zero magnetic field, the Cr^{3+} spins align antiferromagnetically along the (111) easy axis where the

Received: July 30, 2012
Published: October 23, 2012

dx.doi.org/10.1021/ic301671a | *Inorg. Chem.* 2012, 51, 11745−11752

magnetic moments alternate in a $(+-+-)$ array for the *bacd* chromium sites in the corundum structure.[30] This makes the material interesting for devices involving the exchange bias effect.[31] Additionally, Cr_2O_3 displays piezomagnetic (a pronounced stress-induced magnetization) and magnetoelectric effects, making it a promising component for future spintronic applications.[32] The fraction of the surface atoms increases when particle (crystallite) sizes of the magnetic materials decrease, and thus the surface and interface interactions become more important for nanostructured materials.[33] Our recent magnetic study on a series of nanocast AF metal oxides (Co_3O_4, CoO, Cr_2O_3) indicated that nanocast AF metal oxides consist of an AF core and a diluted AF shell.[34,35]

Here we demonstrate the preparation of a series of highly ordered mesoporous Cr_2O_3 from decomposition of chromium(VI) oxide via nanocasting by using cubic ordered mesoporous silica as a hard template. The effect of calcination temperature on structure, textural parameters and magnetic behavior of Cr_2O_3 has been investigated. Unexpectedly, we observed that changes in the lattice parameters lead to changes in the value of the Néel temperature and the spin-flop transition takes place at a smaller applied magnetic field than in the bulk.

2. EXPERIMENTAL SECTION

Mesoporous KIT-6 was prepared according to the literature.[36] Briefly, 13.5 g of surfactant (Pluronic 123, $EO_{20}PO_{70}EO_{20}$) was dissolved in a solution of 487.5 g of distilled water and 26.1 g of concentrated HCl (37%). 13.5 g of *n*-butanol was added to the homogeneous solution at 35 °C. After 1 h of stirring, 29 g of TEOS (tetraethoxysilane) was added to the solution and stirred at this temperature for 24 h. Subsequently, the mixture was aged (without stirring) at 100 °C for another 24 h. The white solid product was filtered, dried at 90 °C and finally calcined at 550 °C for 6 h.

Mesoporous Cr_2O_3 was prepared by the decomposition of CrO_3 using KIT-6 as the hard template. Two grams of CrO_3 (***Caution!*** *Suspected to be carcinogenic, very toxic T+ classification*) was dissolved in 20 mL of water (1 M solution) and added to 2 g of KIT-6. The mixture was stirred for 3 h at room temperature, and the water was thereafter evaporated at 70 °C. The composite was calcined at different temperatures for 6 h (400, 475, 550, 625, 700, 775 °C). Finally, the silica template was removed using 2 M NaOH aqueous solution, followed by several washes with water and drying at 50 °C.

For characterization, X-ray powder patterns (XRD) of all the samples were recorded on a Stoe STADI P Bragg–Brentano diffractometer with Cu Kα radiation and a secondary monochromator. For the low-temperature *in situ* X-ray powder diffraction experiments, the powders were prepared in glass capillaries of 0.5 mm diameter. The measurements were performed on a Stoe STADI P transmission diffractometer, equipped with a primary Ge monochromator and a linear position sensitive detector. For cooling and heating of the samples a Cryostream Plus system (Oxford Cryosystems, 700 series) was used. The system allows a temperature control between 80 and 500 K. The temperature stability of the system is given as 0.1 K. The wavelength used was Mo Kα_1 (0.70926 Å). Lattice parameters were determined from structure refinements by the Rietveld method.[37] The particle sizes were determined by profile fitting methods implemented in the STOE WinXPOW software package considering the instrumental contribution.[38] The module "Size/Strain" allows the user to calculate crystallite size and microstrain from peak widths. The algorithms provided profile decomposition into Lorentz and Gauss portions and are based on the variation of the integral breadth over 2θ.

Nitrogen adsorption isotherms were measured with an ASAP 2010 adsorption analyzer (Micromeritics) at liquid nitrogen temperature. Prior to the measurements, the samples were degassed at a temperature of 150 °C for 10 h. Total pore volumes were determined using the adsorbed volume at a relative pressure of 0.97. BET (Brunauer–Emmett–Teller) surface area was estimated from the relative pressure range 0.06 to 0.2. Pore size distribution (PSD) curves were calculated by the BJH (Barrett–Joyner–Halenda) method from the desorption branch. Transmission electron microscopy (TEM) images of samples were obtained with an H-7500 microscope (Hitachi) equipped with a cold field emission gun. Samples were dry prepared on a lacey carbon grid. High resolution scanning electron microscopy (HR-SEM) and scanning transmission electron microscopy (STEM) images of the samples were taken using a Hitachi S-5500 ultrahigh resolution cold field emission scanning electron microscope operated at 30 kV. All samples were prepared on a lacey carbon film supported by a copper grid. The obtained images were analyzed using the Scandium 5.0 software package from Soft Imaging System GmbH. The magnetic properties were investigated by means of magnetization measurements obtained using a superconducting quantum interference device (SQUID) magnetometer in the 2–400 K temperature range with the applied fields up to 50 kOe. The samples were measured in powder form in a plastic capsule and a glass holder. The magnetic data are normalized to the total weight of the sample.

3. RESULTS AND DISCUSSION

Structure, morphology and textural parameters of nanocast materials are affected by several factors such as type of hard template, loading steps and amount of precursor, drying procedure and calcination temperature. The porosity and textural parameters of nanocast Cr_2O_3 were investigated by nitrogen physisorption, and the nitrogen adsorption–desorption isotherms and the pore size distribution for cubic ordered

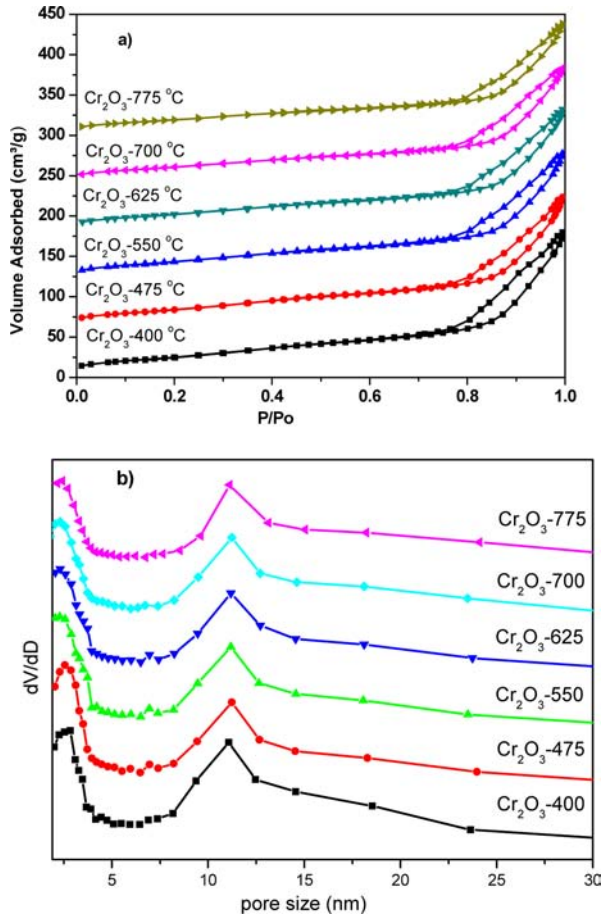

Figure 1. Nitrogen adsorption–desorption isotherms (with an offset value of 60 cm^3/g) (a) and corresponding pore size distributions calculated from desorption branch by BJH method for nanocast Cr_2O_3 heat treated at various temperatures (b).

dx.doi.org/10.1021/ic301671a | *Inorg. Chem.* 2012, 51, 11745–11752

Table 1. Textural Parameters of Nanocast Cr_2O_3 Samples Calculated from N_2-Sorption Measurements

sample	BET, m^2/g	pore volume, cm^3/g
Cr_2O_3-400 °C	92.0	0.235
Cr_2O_3-475 °C	88.2	0.207
Cr_2O_3-550 °C	87.0	0.204
Cr_2O_3-625 °C	82.1	0.194
Cr_2O_3-700 °C	77.3	0.187
Cr_2O_3-775 °C	72.3	0.177

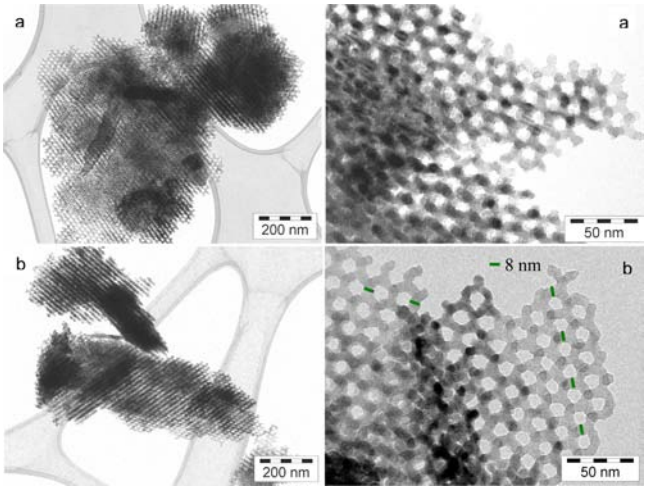

Figure 2. TEM images of ordered mesoporous Cr_2O_3-400 °C (a) and Cr_2O_3-775 °C (b, 8 nm scale bar indicates crystallite size of Cr_2O_3).

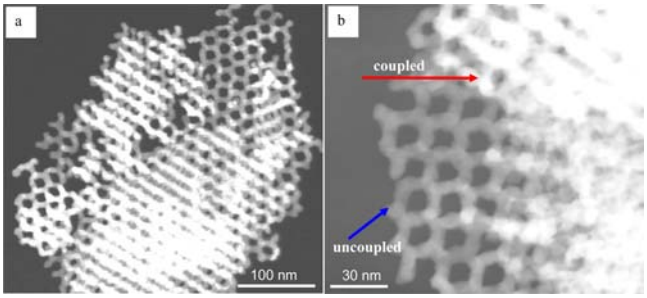

Figure 3. HR-SEM images of nanocast Cr_2O_3-775 °C (a, b) presenting the coupled and the uncoupled structure of the material.

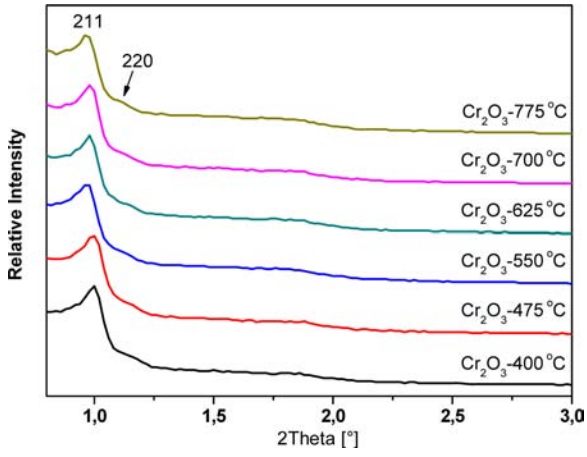

Figure 4. Low angle XRD patterns of mesoporous Cr_2O_3 treated at various temperatures.

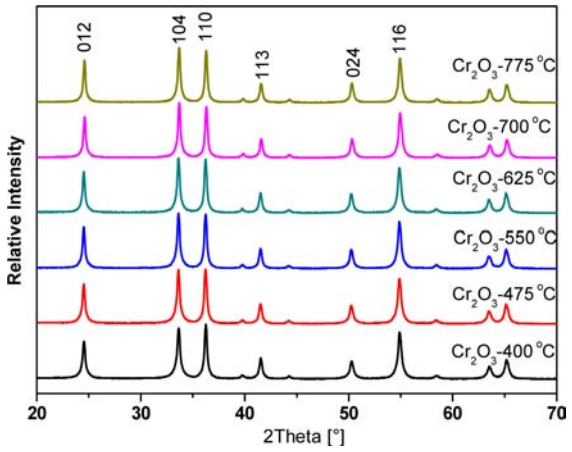

Figure 5. Wide angle XRD patterns of mesoporous Cr_2O_3 treated at various temperatures.

mesoporous Cr_2O_3 are presented in Figure 1. All isotherms are of type IV, showing the typical hysteresis loop of mesoporous materials or metal oxides prepared by the hard templating method. The pore size distribution calculated from desorption isotherms by the BJH method shows a bimodal pore system, with maxima located at 2.5 and 11 nm. The first peak (2.5 nm) is in good agreement with the wall thickness of the KIT-6 (~3 nm) template. As it is known, KIT-6 is composed of two sets of interpenetrating mesopore systems that are connected to each other through micropores in the silica walls, as in SBA-15. When Cr_2O_3 oxide grows within the pores of KIT-6 homogenously, a replica with coupled subframeworks is obtained, which has one type of pore and thus a monomodal pore size distribution. In this case, the nanocast material has a wall thickness equivalent to pore size (~8 nm) of KIT-6 and a pore size corresponding to the wall thickness (~3 nm) of the KIT-6 hard template. On the other hand, Cr_2O_3 can also grow in only one channel system of the KIT-6 template, which results in an uncoupled mesoporous structure that has a larger pore size, equivalent to the dimensions of the walls plus a pore of KIT-6. Earlier studies also indicated that when metal oxides only grow in one of the channel systems of KIT-6, nanocast metal oxides show a bimodal pore size distribution.[7,11,39] Similar effects were also described for the replication of the pore system of MCM-48 by Pt.[40,41]

Textural parameters of the nanocast materials that are relatively important for the material's application can be controlled to a certain extent by varying the reaction conditions. In Table 1, the textural parameters of Cr_2O_3 are summarized. Cr_2O_3-400 °C and Cr_2O_3-775 °C have BET surface areas of 92 and 72 $m^2\ g^{-1}$, and total pore volumes of 0.235 and 0.177 $cm^3\ g^{-1}$, respectively. With increasing calcination temperature, surface area and total pore volume of the nanocast Cr_2O_3 decrease slightly.

The structure and morphology of nanocast Cr_2O_3 were further investigated with microscopy techniques. TEM images of cubic ordered mesoporous Cr_2O_3-400 °C and Cr_2O_3-775 °C are displayed in Figure 2. Highly ordered mesoporous structures of materials can be clearly seen in the micrographs. The average crystallite size was estimated to be 8 ± 1 nm. Besides the ordered mesoporous Cr_2O_3, some bulk material was also observed by TEM analysis. No significant structural changes were detected in the TEM images, if the calcination temperature was increased from 400 to 775 °C. In both cases,

dx.doi.org/10.1021/ic301671a | Inorg. Chem. 2012, 51, 11745−11752

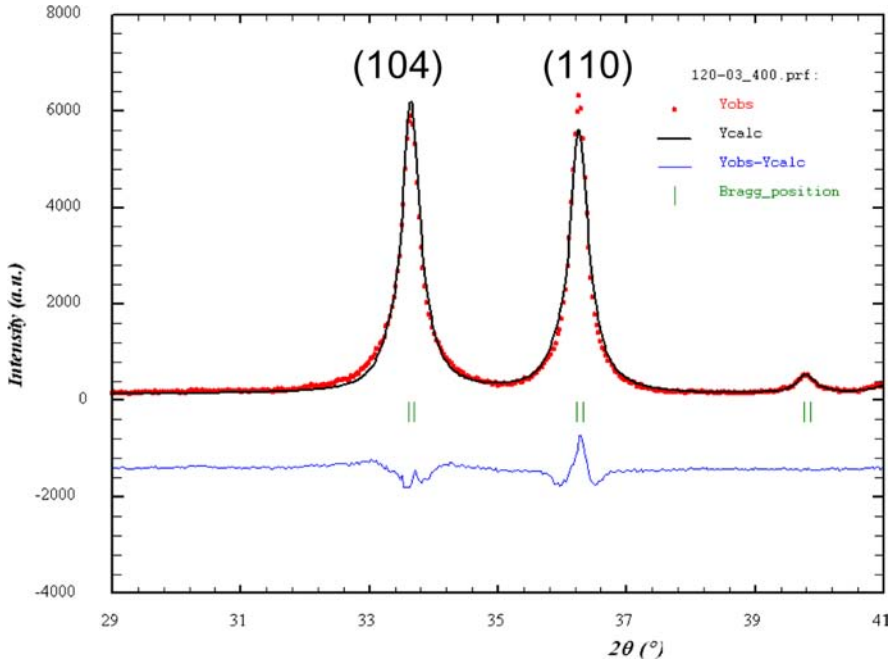

Figure 6. Section of the final structure refinement plot of nanocast Cr_2O_3 calcined at 400 °C.

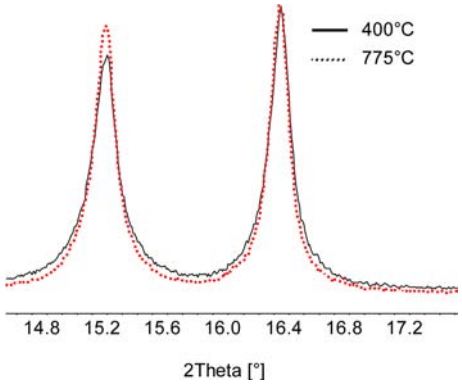

Figure 7. Differences of peak width prove different crystal sizes for nanocast Cr_2O_3 samples calcined at different temperatures.

the images show a mixture of coupled and uncoupled subframeworks. The pore size of the uncoupled subframework structure is estimated to be around 11 nm, in good agreement with N_2-sorption measurements (Figure 1b).

High resolution scanning electron microscopy (HR-SEM) is a powerful analytical technique to study the morphology and surface of the materials. HR-SEM images of Cr_2O_3-775 °C are presented in Figure 3. The material contains domains of the Cr_2O_3 particles, which are in the range of 200−600 nm. The average primary crystallite size is estimated at around 8 nm. Similar to TEM, SEM images indicate that the material consists of coupled (i.e., the two pore systems of the template are filled homogenously) and uncoupled (i.e., only one of the pore system of KIT-6 is filled) subframeworks (Figure 3b).

The mesoscale ordering of the synthesized template free Cr_2O_3 replicas was investigated with low angle XRD (Figure 4). All patterns indicate the (211) and (220) reflections which are characteristic for the 3D cubic structure that is nanocast from KIT-6 hard template. The synthesis of well structured material is facilitated by the high solubility of chromium(VI) oxide in water that facilitates the achievement of high loadings of the precursor into KIT-6 in one impregnation step. After calcination and removal of silica, highly ordered Cr_2O_3 replicas can be obtained.

Decomposition of chromium(VI) oxide can result in the formation of intermediate products such as Cr_3O_8, Cr_2O_5 and CrO_2. Depending on the applied atmosphere, temperature and heating time, different products can be formed. Without special measures, such as increased oxygen pressure, Cr_2O_3 is the most stable and thus favored phase of chromium oxide at high temperature. In the following, the effect of the calcination temperature on the structure of the nanocast Cr_2O_3 will be discussed. The wide-angle X-ray diffraction patterns of cubic ordered mesoporous Cr_2O_3 calcined at various temperatures are shown in Figure 5.

The qualitative analysis reveals a change of the intensity ratio of the (104) and (110) reflections with increasing calcination temperature. The Rietveld refinement plot of the sample calcined at 400 °C displays not only a misfit of intensities between observed and calculated data but also a mismatch of the fitted peak shape (Figure 6). The measured intensity of the (110) reflection is higher than the intensity calculated from crystal structure data. This observation goes along with the fact that the width of the (110) reflection is smaller than the width of the neighboring reflections. The intensity mismatch can be explained by a pronounced preferred orientation of the crystal morphology for samples calcined at low temperatures. The microstructural properties cause an anisotropic broadening of peaks.

Analysis of the individual reflections shows that reflections representing the direction of the crystallographic *c*-axis indicate larger dimensions in this direction. With increasing calcination temperatures, the dimensions along the *c*-axis do not change significantly, whereas the crystals start to grow in the other directions. In addition to the anisotropic peak broadening, all reflections have peak shapes that cannot be explained by a single Lorentzian type profile. This type of peak shape, which is difficult to simulate, indicates a broad particle size distribution. Very broad reflections generated by small particles and narrow

dx.doi.org/10.1021/ic301671a | *Inorg. Chem.* 2012, 51, 11745−11752

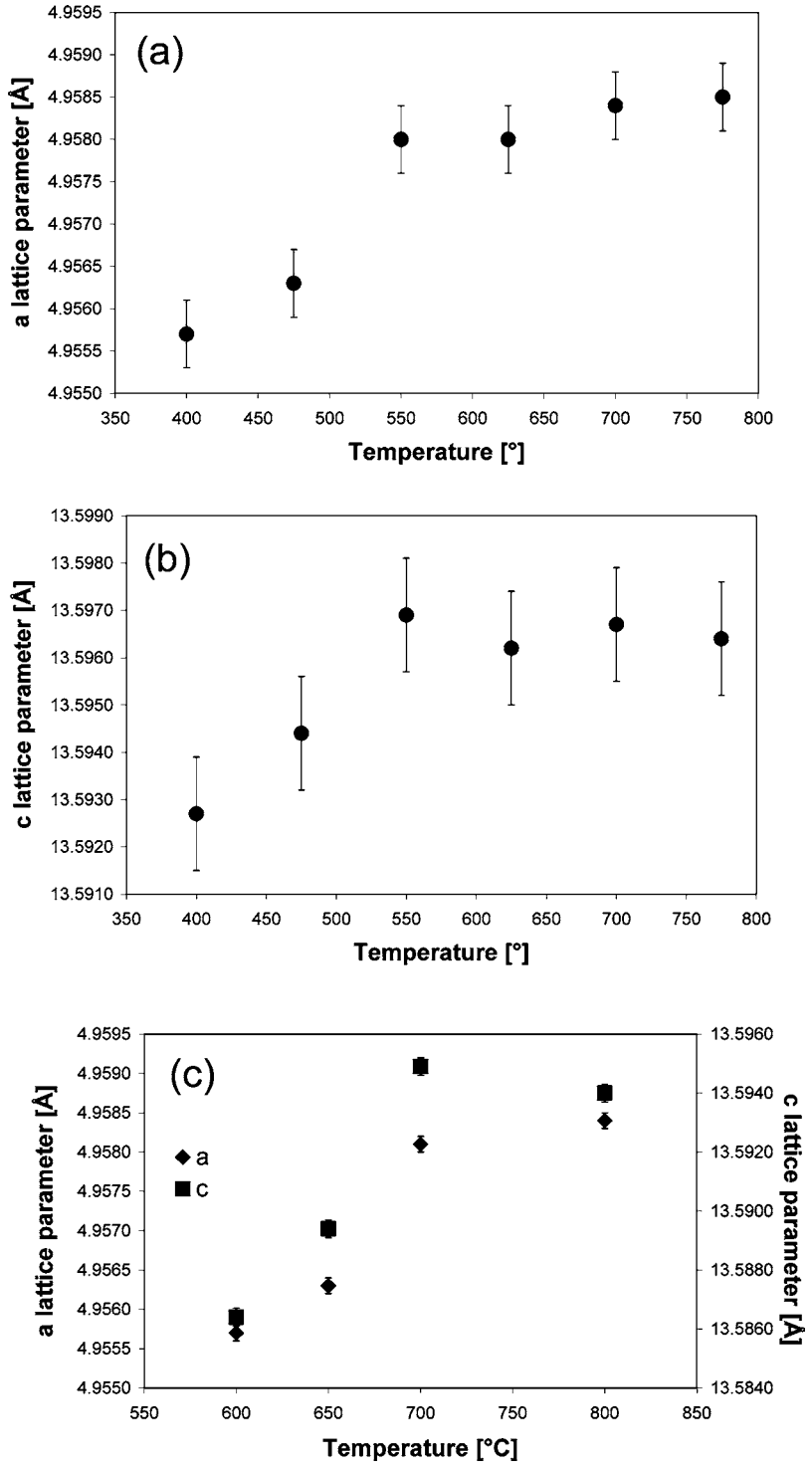

Figure 8. Change of (a) the *a* lattice parameter, (b) the *c* lattice parameter of nanocast Cr_2O_3, and (c) the *a* and *c* lattice parameters of bulk Cr_2O_3 with various calcination temperatures.

reflections caused by larger crystals overlap and result in a very typical peak profile. In spite of these difficulties, diffraction data were used to determine mean crystal sizes. Small changes of the reflection width with temperature indicate different mean particle sizes (Figure 7). The mean crystal size after calcination at 400 °C is determined to be about 16 nm whereas the mean crystal size of the sample calcined at 775 °C is about 20 nm. These results do not completely correspond to the particle size of about 8 nm determined from the TEM images (see below). TEM, however, is not representative for the whole sample. Survey TEM images confirm the presence of larger Cr_2O_3 particles beside the mesoporous areas consisting of small Cr_2O_3 particles, which correlates quite well with the XRD results.[42]

For the samples calcined at different temperatures, structure refinements were conducted. Changes of lattice parameters with calcination temperatures, determined from structure refinements, are shown in Figure 8. Both *a* and *c* lattice parameters increase with calcination temperature and reach a

dx.doi.org/10.1021/ic301671a | *Inorg. Chem.* 2012, 51, 11745−11752

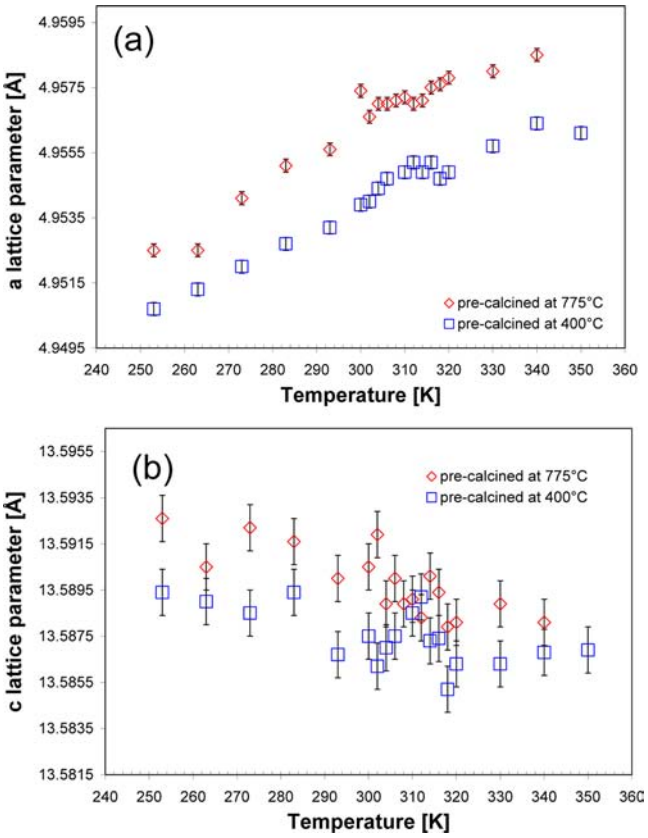

Figure 9. Development of (a) the *a* lattice parameters and (b) the *c* lattice parameters of nanocast Cr_2O_3 with temperature. Results are obtained from the *in situ* diffraction data.

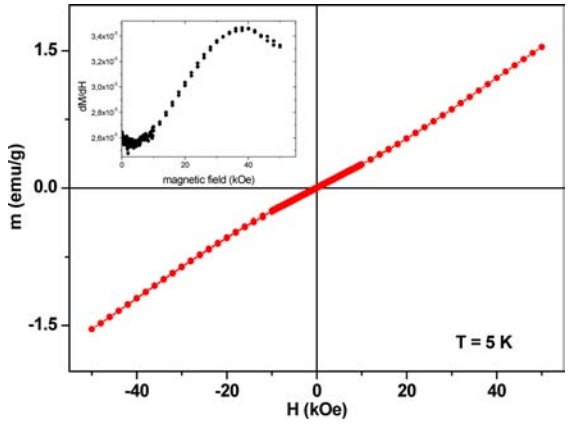

Figure 10. Magnetization versus field recorded at T = 5 K for the sample calcinated at 775 °C. In the inset, the field derivative of magnetization is plotted. The peak in dM/dH is giving the spin-flop field value.

plateau above 600 °C (Figure 8a,b); this is a quite unusual behavior for oxide materials. For very small particles on the order of a few nanometers in size, lattice parameters are known to deviate from the bulk value.[43] However, the particle sizes of 16−20 nm observed here are too large to explain the change of the unit cell size. Control experiments on bulk Cr_2O_3 with particle sizes of already 60 nm at 600 °C revealed a similar increase of the lattice parameters with thermal treatment (Figure 8c). An increase of lattice parameters with calcination temperature was observed for CeO_2 and in a previous paper

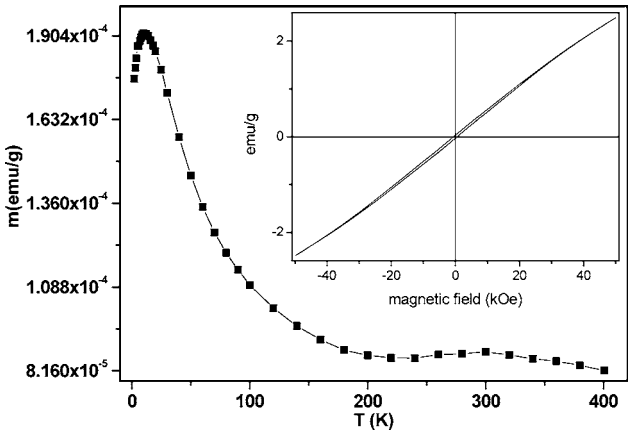

Figure 11. The zero-field-cooled magnetization measured at 100 Oe for the sample calcined at 400 °C. In the inset, the ZFC hysteresis loop recorded at T = 5 K is shown.

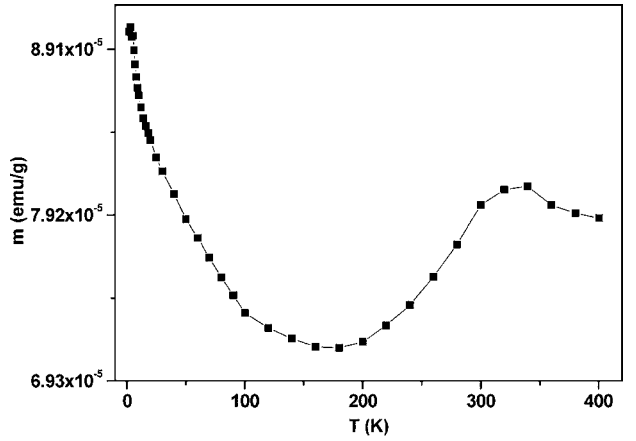

Figure 12. The zero-field-cooled magnetization measured at 100 Oe for the sample calcined at 775 °C.

also for Cr_2O_3, but the observation is not fully understood.[44,45] *In situ* low temperature X-ray diffraction experiments were performed in the temperature range between 253 and 350 K. As starting materials the samples precalcined at 400 and 775 °C were used (Figure 9). For both series, an increase of the *a* lattice parameter with temperature is observed, whereas the *c* lattice parameter slightly decreases. This is in accordance with data shown in the literature.[46] The lattice parameters determined *in situ* for the sample precalcined at 400 °C remain smaller than the unit cell parameters of the sample precalcined at 775 °C. Close to the Néel temperature the linear increase of the *a* parameter gets disturbed, which is much more pronounced for the *c* parameter.

Magnetic nanostructures often show properties differing from the magnetic properties of bulk material. Such aspects of the Cr_2O_3 nanostructure will be addressed in the following. Figure 10 shows the magnetization hysteresis loop measured at 5 K for a Cr_2O_3 nanostructure calcined at 775 °C. As one expects for a system of antiferromagnetic nanoparticles, the magnetization versus field curve is nearly linear and does not show any magnetic saturation. One interesting feature is the change in the curvature of the magnetization curve. This phenomenon can be related to a spin-flop transition. It is well-known that in antiferromagnetic materials a spin-flop transition occurs when larger fields are applied and the sublattice

dx.doi.org/10.1021/ic301671a | *Inorg. Chem.* 2012, 51, 11745−11752

magnetization becomes nearly perpendicular to the applied magnetic field. At the spin-flop transition the orientation of the spins changes from the direction parallel to the c axis to the direction perpendicular to it. The critical field, H_{sf}, for spin flopping, in terms of the molecular exchange field H_E and the anisotropy field H_A, is given by $H_{sf} = (2H_EH_A)^{1/2}$. Since both the interparticle exchange interactions and magnetic anisotropy are size dependent, a different behavior compared to bulk material might be expected. The spin flop for bulk Cr_2O_3 occurs at 6 T at 4.2 K and at 12.1 T at 305 K.[47] Due to surface effects, crystal defects and/or deviation from stoichiometry, for nanoparticles one expects a reduction of the spin-flop field with respect to the bulk value. In the inset of Figure 10 the differential magnetization dM/dH versus H is shown. The spin-flop is taken as the field at which a maximum occurs in the derivative of M versus H curves (dM/dH). Based on this, for the Cr_2O_3 nanostructure a spin-flop transition at 5 K was measured at a field of 3.6 T, which is much smaller than the value observed for the bulk. At room temperature no spin-flop transition was detected in magnetic fields up to 5 T. Furthermore, we have measured the transition field for smaller particles with a diameter of around 5 nm (data not shown). We observed that H_{sf} decreases with decreasing particle size. For 5 nm particles the spin-flop transition was observed at around 3 T. This reduction of the spin-flop transition field with decreasing particle size can be related to a strong decrease in the magnetic anisotropy constant, which has in turn been attributed—among others—to the disorder induced in the surface.[30] A similar effect has been reported for acicular hematite nanoparticles where the authors claim a reduction of the spin-flop field with decreasing particle size.[48]

We now focus our discussion on the temperature dependence of magnetization for two samples calcined at 400 and 775 °C. The zero-field-cooled (ZFC) magnetization curves measured in the presence of a 100 Oe dc magnetic field as a function of temperature in the temperature range 2−400 K are shown in Figures 11 and 12. In Figure 11, the results for the Cr_2O_3 nanostructure calcined at 400 °C are presented.

One can distinguish two magnetic features in the variation of the magnetization with the temperature. One is the broad peak around 310 K, which is associated with the Néel temperature transition. For bulk Cr_2O_3 a Néel temperature around 307 K has been reported.[31] The other feature is the additional peak observed at T = 10 K that can be interpreted as the blocking temperature of very small Cr_2O_3 nanoparticles. As discussed before, the XRD results suggest that the samples do not have a narrow size distribution. Thus, it is reasonable to assume that the Néel transition is caused by the bigger particles in the sample while the particles with smaller diameters are blocked around 10 K, showing a weak ferromagnetism below this transition. The contribution of small Cr_2O_3 nanoparticles to the total magnetization is reflected in the inset of Figure 11, where the hysteresis loop recorded at T = 5 K is plotted. A weak ferromagnetic behavior, with a coercivity of about 550 Oe and a shift of the hysteresis loop along the field axis of about 350 Oe, has been measured. Since a perfectly compensated antiferromagnet does not show hysteresis, the weak ferromagnetism is due to the uncompensated surface spins. Numerous studies have shown that the antiferromagnetic nanoparticles often exhibit a net magnetic moment owing to uncompensated surface spins, with the moment becoming larger as the surface-to-volume ratio increases.[49,50] Additionally, superparamagnetic behavior and weak ferromagnetism in Cr_2O_3 nanoparticles have also been reported.[51,52] Figure 12 shows the temperature dependence of the magnetization for the sample calcined at 775 °C. The magnetization decreases with increasing temperature, and at the antiferromagnetic transition a plateau region around 320−350 K is observed. These values of the ordering temperature are much higher than the bulk antiferromagnetic transition. This enhancement of the Néel temperature can be explained based on the results of structural investigations, where a dependence of the lattice parameter on the calcination temperature was observed. As shown in Figure 9, the a lattice parameter for the sample calcined at 775 °C is larger than the a lattice parameter for the sample calcined at 400 °C. This enhancement of the lattice parameter can lead to a shift of the Néel transition to higher temperatures. Further studies need to be carried out to investigate the reasons for this enhancement.

4. CONCLUSION

In this paper we report the structural and magnetic characterization of a series of mesoporous Cr_2O_3 nanostructures fabricated from the decomposition of chromium(VI) oxide using KIT-6 as a hard template. This study brings forth the principal finding that, with increasing calcination temperature, surface area and pore volume of mesoporous Cr_2O_3 decrease slightly. In addition, HR-SEM analysis clearly indicated that the nanostructured materials contain both the uncoupled and the coupled structure. Unexpectedly crystal structure refinement reveals increasing lattice parameters with increasing calcination temperatures. The magnetic studies confirm a significant increase in T_N with respect to the bulk for the sample calcined at elevated temperature and a spin-flop transition at much smaller fields compared to that the bulk.

AUTHOR INFORMATION

Corresponding Author

*E-mail: schueth@mpi-muelheim.mpg.de.

Present Address

[†]Oerlikon Solar, Hauptstrasse 1a, 9477 Trübbach, Switzerland.

Notes

The authors declare no competing financial interest.

ACKNOWLEDGMENTS

We thank Dr. E. Bill and A. Göbels for the SQUID measurements (Max Planck Institute for Bioinorganic Chemistry, Mülheim an der Ruhr, Germany), Dr. C. Lehmann, A. Dreier and H. Bongard for the HR-TEM and HR-SEM images.

REFERENCES

(1) Ryoo, R.; Joo, S. H.; Jun, S. *J. Phys. Chem. B* **1999**, *103*, 7743.
(2) Schmidt, W. *ChemCatChem* **2009**, *1*, 53.
(3) Tiemann, M. *Chem. Mater.* **2008**, 961.
(4) Lu, A. H.; Schüth, F. *Adv. Mater.* **2006**, *18*, 1793.
(5) Wang, Y.; Zhao, D. *Chem. Rev.* **2007**, *107*, 7.
(6) Shi, Y.; Wan, Y.; Zhao, D. *Chem. Soc. Rev.* **2011**, *40*, 3854.
(7) Tüysüz, H.; Lehmann, C. W.; Bongard, H.; Schmidt, R.; Tesche, B.; Schüth, F. *J. Am. Chem. Soc.* **2008**, *130*, 11510.
(8) Yue, W.; Hill, A. H.; Harrison, A.; Zhou, W. *Chem. Commun.* **2007**, 2518.
(9) Jiao, F.; Jumas, J. C.; Womes, M.; Chadwick, A. V.; Harrison, A.; Bruce, P. G. *J. Am. Chem. Soc.* **2006**, *128*, 12905.
(10) Tüysüz, H.; Salabas, E. L.; Weidenthaler, C.; Schüth, F. *J. Am. Chem. Soc.* **2008**, *130*, 280.
(11) Jiao, F.; Hill, A. H.; Harrison, A.; Berko, A.; Chadwick, A. V.; Bruce, P. G. *J. Am. Chem. Soc.* **2008**, *130*, 5262.

(12) Tian, B. Z.; Liu, X. Y.; Yang, H. F.; Xie, S. H.; Yu, C. Z.; Tu, B.; Zhao, D. Y. *Adv. Mater.* **2003**, *15*, 1370.
(13) Jiao, F.; Harrison, A.; Hill, A. H.; Bruce, P. G. *Adv. Mater.* **2007**, *19*, 4063.
(14) Shi, Y.; Guo, B.; Corr, S. A.; Shi, Q.; Hu, Y. S.; Heier, R. K.; Chen, L.; Seshadri, R.; Stucky, G. D. *Nano Lett.* **2009**, *9*, 4215.
(15) Laha, S.; Ryoo, R. *Chem. Commun.* **2003**, 2138.
(16) Roggenbuck, J.; Tiemann, M. *J. Am. Chem. Soc.* **2005**, *127*, 1096.
(17) Lai, X.; Li, X.; Geng, W.; Tu, J.; Li, J.; Qiu, S. *Angew. Chem., Int. Ed.* **2007**, *46*, 738.
(18) Tüysüz, H.; Yong, L.; Weidenthaler, C.; Schüth, F. *J. Am. Chem. Soc.* **2008**, *130*, 14108.
(19) Tüysüz, H.; Weidenthaler, C.; Schüth, F. *Chem.—Eur. J.* **2012**, *18*, 5080.
(20) Rumplecker, A; Kleitz, F.; Salabas, E. L.; Schüth, F. *Chem. Mater.* **2007**, *19*, 485.
(21) Sun, X.; Shi, Y.; Zhang, P.; Zheng, C.; Zheng, X.; Zhang, F.; Zhang, Y.; Guan, N.; Zhao, D.; Stucky, G. D. *J. Am. Chem. Soc.* **2011**, *133*, 14542.
(22) Cherian, M.; Rao, M. S.; Yang, W.-T.; Jehng, J.-M.; Hirt, A. M.; Deo, G. *Appl. Catal., A* **2002**, *233*, 21.
(23) York, S. C.; Cox, D. F. *J. Phys. Chem. B* **2003**, *107*, 5182.
(24) Zhu, K.; Yue, B.; Zhou, W.; He, H. *Chem. Commun.* **2003**, 98.
(25) Jiao, K.; Zhang, B.; Yue, B.; Ren, Y.; Liu, S.; Yan, S.; Dickinson, C.; Zhou, W.; He, H. *Chem. Commun.* **2005**, 5618.
(26) Liu, H.; Du, X.; Xing, X.; Wang, G.; Qiao, S. H. *Chem. Commun.* **2012**, 865.
(27) Shi, Y.; Wan, Y.; Zhang, R.; Zhao, D. Y. *Adv. Funct. Mater.* **2008**, *18*, 2436.
(28) Sinha, A. K.; Suzuki, K. *Angew. Chem., Int. Ed.* **2005**, *44*, 271.
(29) Hill, A. H.; Harrison, A.; Dickinson, C.; Zhou, W.; Kockelmann, W. *Microporous Mesoporous Mater.* **2010**, *130*, 280.
(30) Tobia, D.; Winkler, E.; Zysler, R. D.; Granada, M.; Troiani, H. E. *Phys. Rev. B* **2008**, *78*, 104412.
(31) McGuire, T. R.; Scott, E. J.; Grannis, F. H. *Phys. Rev.* **1956**, *102*, 1000.
(32) Sahoo, S.; Binek, C. *Philos. Mag. Lett.* **2007**, *87*, 259.
(33) Tüysüz, H.; Salabas, E. L.; Bill, E.; Bongard, H.; Spliethoff, B.; Lehmann, C. W.; Schüth, F. *Chem. Mater.* **2012**, *24*, 2493.
(34) Benitez, M. J.; Petracic, O.; Salabas, E. L.; Radu, F.; Tüysüz, H.; Schüth, F.; Zabel, Z. *Phys. Rev. Lett.* **2008**, *101*, 097206.
(35) Benitez, M. J.; Petracic, O.; Tüysüz, H.; Schüth, F.; Zabel, H. *EPL* **2009**, *88*, 27004.
(36) Kleitz, F.; Choi, S. H.; Ryoo, R. *Chem. Commun.* **2003**, 2136.
(37) Rodriguez-Carvajal, J. FULLPROF: A Program for Rietveld Refinement and Pattern Matching Analysis. In *Abstracts of the Satellite Meeting on Powder Diffraction of the XV Congress of the IUCr*, Toulouse, France, 1990; p 127.
(38) WinXPOW Version 2.21, Copyright STOE & Cie GmbH Darmstadt, Germany, 2007.
(39) Dickinson, C.; Zhou, W.; Hodgkins, R. P.; Shi, Y.; Zhao, D.; He, H. *Chem. Mater.* **2006**, *18*, 3088.
(40) Hyun, J. S.; Ryoo, R.; Liu, Z.; Terasaki, O. *J. Am. Chem. Soc.* **2001**, *123*, 1246.
(41) Terasaki, O.; Ohsuna, T. *Top. Catal.* **2003**, *24*, 13.
(42) Weidenthaler, C. *Nanoscale* **2011**, *3*, 792.
(43) Lamber, R.; Wetjen, S.; Jaeger, N. I. *Phys. Rev. B* **1995**, *51*, 10968.
(44) Morris, V. N.; Farrell, R. A.; Sexton, A. M.; Morris, M. A. *J. Phys. (Paris)* **2006**, *26*, 119.
(45) Banobre-López, M.; Vázquez-Vázquez, C.; Rivas, J.; López-Quintela, M. A. *Nanotechnology* **2003**, *14*, 318.
(46) Greenwald, S. *Nature* **1956**, *177*, 286.
(47) Shapira, Y. *Phys. Rev.* **1969**, *187*, 734.
(48) Zysler, R. D.; Fiorani, D.; Testa, A. M.; Suber, L.; Agostinelli, E.; Godinho, M. *Phys. Rev. B* **2003**, *68*, 212408.
(49) Salabas, E. L.; Rumplecker, A.; Kleitz, F.; Radu, F.; Schüth, F. *Nano Lett.* **2006**, *6*, 2977.
(50) Mørup, S.; Madsen, D. E.; Frandsen, C.; Bahl, C. R. H.; Hansen, M. F. *J. Phys.: Condens. Matter* **2007**, *19*, 213202.
(51) Makhlouf, S. A. *J. Magn. Magn. Mater.* **2004**, *272*−*276*, 1530.
(52) Vázquez-Vázquez, C.; Bañobre-López, M.; López-Quintela, M. A.; Hueso, L. E.; Rivas, J. *J. Magn. Magn. Mater.* **2004**, *272*−*276*, 1547.